



Ultrahigh density plasmonic hot spots with ultrahigh electromagnetic field for improved photocatalytic activities



Tung-Han Yang^a, Yeu-Wei Harn^a, Ming-Yang Pan^b, Li-De Huang^c, Miao-Chun Chen^a, Ben-Yuan Li^c, Pei-Hsuan Liu^a, Po-Yen Chen^a, Chun-Cheng Lin^c, Pei-Kuen Wei^b, Lih-Juann Chen^a, Jenn-Ming Wu^{a,*}

^a Department of Materials Science and Engineering, National Tsing Hua University, Hsinchu 30013, Taiwan

^b Research Center for Applied Sciences, Academia Sinica, Taipei 115, Taiwan

^c Department of Chemistry, National Tsing Hua University, Hsinchu 30013, Taiwan

ARTICLE INFO

Article history:

Received 3 June 2015

Received in revised form 29 July 2015

Accepted 6 August 2015

Available online 10 August 2015

Keywords:

Plasmonic hot spot

Photocatalyst

Surface plasmon resonance

Finite-difference time-domain

Photodegradation

ABSTRACT

Plasmonic hot spots located among closely dispersed plasmonic nanoparticles (NPs) are intensively studied for efficient conversion of solar to chemical or electrical energy applications. Here, a successful method to synthesize high-density unaggregated plasmonic Ag or Au NPs (AgNPs or AuNPs) onto nanostructured semiconductors with 3D densely organized NPs is demonstrated. The densely dispersed plasmonic AgNPs or AuNPs are assembled chemically on the entire surface of the ZnO nanorods through bifunctional thioctic acid bridging linkers. The fabricated NPs possessing small interparticle gaps generate numerous plasmonic hot spots which boost catalytic activities of the photocatalysts. As depicted by exact 3D finite-difference time domain simulations, the electromagnetic fields are magnified exponentially among interparticle gaps, hot spots, due to the plasmonic coupling effects of the neighboring AgNPs. The electromagnetic fields are strengthened by decreasing the interparticle spacing of coupled AgNPs. It is consistent with the result that the photocatalytic reaction rate increases non-linearly with the Ag content under full-spectrum light irradiation. Using the spectral characterizations and electromagnetic field simulations, we unambiguously confirm the enhancement of photoactivity due to coupling of plasmonic hot spot effect to nanostructured semiconductors. Moreover, diverse heterostructures based on the plasmonic NPs on various ZnO nanostructures (films, nanorod arrays, branched nanowires, and mesoporous structures) or functional materials (CuInGaSe₂ absorber films, multiferroic BiFeO₃ films, visible-light photoactive Cu₂S and CdS nanorods) are successfully fabricated using the present synthesis methodology.

© 2015 Elsevier B.V. All rights reserved.

1. Introduction

Recently, surface plasmon resonance (SPR) is intensively studied for application in solar energy harvesting, conversion, and storage as well as environmental pollutant purification [1–8]. Plasmonic nanostructures especially for the Ag or Au nanoparticles (AgNPs or AuNPs) support the formation of SPRs in response to a visible light flux and localize the electromagnetic energy to their surfaces [9]. For visible-light-driven photocatalytic applications, the interaction of the plasmonic AgNPs or AuNPs with their neighboring semiconductor allows for an enhanced generation of electron–hole pairs in the near-surface region of the semiconductor [10]. These charge carriers are readily separated and easily migrate to the surface (short exciton diffusion length), where they can perform photo-

catalytic transformations. The SPR-induced enhancement in the generation rate of electron–hole pairs through the near-field mechanism is dependent on the intensity of local electromagnetic fields [11–13]. Both experimental and theoretical works have demonstrated that a high local electromagnetic field leads to increased light absorption and effective generation of electron–hole pairs at the surface of the Ag-TiO₂ [14], Ag-Cu₂O [15], Ag-AgCl [16], Ag-ZnO [17], Au-TiO₂ [18–21], Au-Fe₂O₃ [22–25], Au-Si [26], Au-SiO₂ [27], Au-GaP [28], or Au-ZnO [29] heterostructures for plasmonic enhancement of photocatalytic reactions.

Interaction of light with nanostructures gives rise to a variety of interesting optical phenomena in nanoscale. SPR concentrates the light flux (the energy of incoming photons) in small volumes surrounding the nanostructure. Duan and coworkers [30] reported that the calculated electromagnetic field enhancement (E^2/E_0^2) of more than 1 order of magnitude can be achieved around the plasmonic AgNPs or AuNPs near the surface of the Si photodiodes. The enhancement quickly decays to a much smaller enhancement

* Corresponding author.

E-mail address: jmwu@mx.nthu.edu.tw (J.-M. Wu).

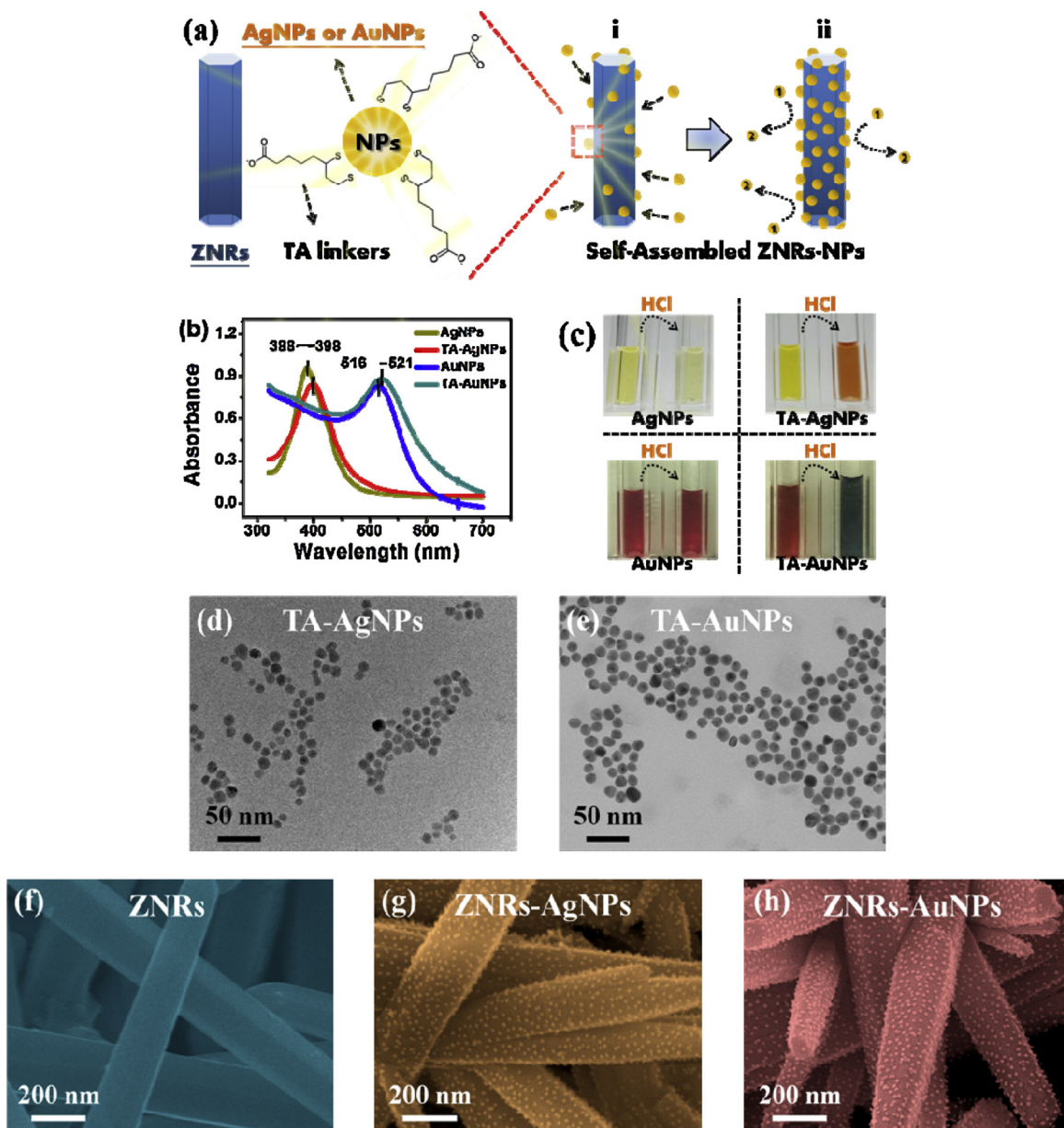


Fig. 1. (a) Schematic of the synthesis methodology for ZNRs-NPs heterostructures using TA linkers. (b) Optical absorption spectra of AgNPs and AuNPs before and after modification with TA. (c) Photographs of AgNPs, AuNPs, TA-functionalized AgNPs, and TA-functionalized AuNPs before and after adding HCl solution. TEM images of (d) TA-functionalized AgNPs and (e) TA-functionalized AuNPs. SEM images of (f) ZNRs, (g) ZNRs-AgNPs (30 wt.%), and (h) ZNRs-AuNPs (30 wt.%) heterostructures. (For interpretation of the references to color in the text, the reader is referred to the web version of this article.)

factor of 1.5–5 at a distance of 15 nm from the plasmonic NPs. The wavelength and the intensity of the SPR of metal particles are highly sensitive to the metal species, size, shape, interparticle spacing, and the dielectric environment [31,32]. Most importantly, numerous experimental and theoretical efforts have confirmed that the local “hot spot”, which locates in the gap region between closely dispersed plasmonic particles in 2D-patterned plasmonic particle arrays, can enhance the local electromagnetic field by several orders of magnitude higher than that by isolated particles [3,21,33–37]. Very recently, Mangelson et al. [38] developed a procedure for synthesizing Au nanorod dimers embedded within TiO_2 sheets as case study for the incorporation of plasmonically active materials into generic semiconductor films. They showed that this composite amplifies the electric field of incident light within the gap between nanorod segments. These studies stimulated keen interests in fabricating 3D heterostructures composed of closely

dispersed plasmonic NPs decorating on the surface of semiconductor nanostructures, aiming for high number density plasmonic hot spots with high electromagnetic field to overcome the limited efficiency of photocatalysts and photovoltaic devices.

With the pertinent motivation, we firstly develop a controlled synthesis of remarkable 3D photocatalysts composed of high-density unaggregated plasmonic AgNPs or AuNPs chemically bound to one dimensional ZnO nanorods (ZNRs) through thioctic acid (TA) as a bifunctional molecular linker, as shown in Fig. 1a. The hence successfully fabricated new materials of plasmonic metal–semiconductor 3D heterostructures have high number density of plasmonic hot spots with ultrahigh electromagnetic field. As depicted by 3D finite-difference time domain (FDTD) simulations, significant incoming photon confinement and enhancement around the metal–semiconductor interfacial plasmon hot spots contribute to efficient conversion of light energy to electron–hole

pairs. We unambiguously confirm the enhancement of photocatalytic activity due to coupling of plasmonic hot spot effect to nanostructured semiconductors. It thus contributes mainly to the SPR-induced enhancement of photocatalytic activity. Additionally, photoconductive measurements of AgNPs- and AuNPs-decorated single ZnO nanorod agree well with the discussion on the plasmonic enhancement of photoactivity. Moreover, various hybrid structures based on the plasmonic NPs and diverse nanostructures or functional materials can be successfully constructed using the bifunctional TA linkers. The plasmonic NPs can be stably anchored on a diverse range of materials with varied surface properties. Multifunctional plasmonic heterostructures adopting the synthesis methodology described in this study will facilitate the current, or even enable new, applications in photocatalysts, photovoltaics, photonic sensors, and so forth, in a controllable and scalable manner.

2. Experimental

2.1. Preparation of ZNRs by a hydrothermal method

$Zn(NO_3)_2 \cdot 6H_2O$ and $C_6H_{12}N_4$ precursors were individually added to deionized water to form two 0.01 M precursor solutions. These two solutions were mixed together in a glass bottle. The glass bottle was then sealed and maintained at 90 °C for 2 h in order to grow ZNRs. After the growth of ZNRs, the sample was removed from the solutions, rinsed with distilled water, and dried at room temperature.

2.2. Synthesis of 10 nm sized TA-AgNPs

A solution of 1.0 mM silver nitrate (60 mL, 10.2 mg, 0.06 mmol) was added dropwise to 2.0 mM sodium borohydride solution (180 mL, 13.62 mg, 0.36 mmol) which was chilled in an ice bath. The reaction mixture was stirred vigorously on a magnetic stir plate. The solution turned light yellow after the addition of 10 mL of silver nitrate. The color became bright yellow when all of the silver nitrate had been added. The entire addition took about ten minutes. To improve the stability of AgNPs, Na citrate (141 mg, 0.48 mmol) was added to the $NaBH_4$ stabilized AgNPs solution. The resulting yellow colloidal silver was stable which could be stored in a transparent vial for several months. To a solution of $NaBH_4$ or citrate stabilized AgNPs (240 mL), of which the basicity was pre-adjusted to pH 11 by 0.5 M NaOH, was added thioctic acid (49.2 mg in 1 mL MeOH, 0.24 mmol) and left for self-assembling for 48 hrs. Excess TA was removed via three cycles of centrifugation and resuspension with H_2O (pH > 11).

2.3. Synthesis of 10 nm sized citrate-stabilized AuNPs (c-AuNPs)

To an aqueous solution (200 mL) of sodium citrate (140 mg, 0.476 mmol) with stirring was added 440 μL of 5% $HAuCl_4 \cdot 3H_2O$ solution (20 mg, 0.051 mmol) at 100 °C. The solution was refluxed for additional 15 mins, then cooled to room temperature and stored in 4 °C for future functionalization.

2.4. Synthesis of 35 nm sized c-AuNPs

To an aqueous solution (200 mL) of $HAuCl_4 \cdot 3H_2O$ (79 mg, 0.2 mmol) with stirring was added 10 mL of 1% sodium citrate (100 mg, 0.34 mol) at 100 °C rapidly. The solution was refluxed for additional 15 mins, then cooled to room temperature and stored in 4 °C for future functionalization.

2.5. Synthesis of 10 nm and 35 nm sized TA-AuNPs

To a solution of c-AuNPs (200 mL), which basicity was pre-adjusted to pH 11 by 0.5 M NaOH, was added thioctic acid (50 mg in 1 mL MeOH, 0.24 mmol) and left for self-assembling for 48 hrs. Excess TA was removed via centrifugation (minispin, Eppendorf; 11000 and 4500 rpm for 10 and 35 nm c-AuNPs, respectively) and resuspension with H_2O (pH > 11) for three times.

2.6. Preparation of chemically assembled ZNRs-AgNPs and ZNRs-AuNPs

The ZNRs were placed in a vial containing TA-functionalized AgNPs or AuNPs, which have been dispersed for 1 h. The ZNRs-AgNPs or ZNRs-AuNPs heterostructures were then washed with distilled water to remove excess TA-functionalized AgNPs or AuNPs.

2.7. Materials characterization

The optical properties were measured by a Hitachi U-3010 spectrometer. A high resolution transmission electron microscope (HRTEM, JEM-3000F) was used to determine structures and phases formed in the samples. The photoluminescence (PL) spectroscopy was gathered by exciting the samples with a continuous wave He-Cd laser (325 nm). The crystalline structures were analyzed by X-ray diffraction (XRD, PANalytical X'Pert Pro). The morphology and chemical composition of the samples were observed with a field-emission scanning emission microscopy (SEM, JEOL-6500). We have used the inductively-coupled plasma mass spectrometry (ICP-MS, Agilent 7500ce) measurements to quantitatively determine the metal loadings. X-ray photoelectron spectroscopy (XPS, VG Scientifi c-Microlab 350) was used to examine the chemical states of the samples. The photoconductive characteristics were analyzed with a semiconductor parameter analyzer (Agilent, B1500A) under full-spectrum light illumination.

2.8. 3D finite-difference time-domain (FDTD) Simulation

We calculated the electromagnetic field distributions 10 nm sized AgNPs or AuNPs which are coated on ZnO surfaces with 5, 10, 15, and 20 nm interparticle gaps. Since it is extremely difficult to precisely probe the molecular length of the bifunctional TA linkers containing the carboxylate groups for ZNRs attachment and thiols as strong AgNPs or AuNPs binding functional groups, we simulated electromagnetic field distributions of the ZNRs-NPs heterostructures without involving the relatively short (should be less than 1 nm) TA molecules. According to the photocatalytic experimental data in the supporting information file, the ZNRs-NPs heterostructure with or without the TA linkers shows almost identical photocatalytic property. Thus, we reasonably believe that the presence of the relatively short TA molecules would not influence the plasmonic interaction of the NPs with their neighboring ZnO semiconductors under light illumination. The electric fields affected by ZnO-NPs immersing in water with refractive index $n=1.333$ simulated by 3D FDTD (Fullwave 6.1, Rsoft) under 410 or 530 nm monochromatic light illuminations. In the simulation, the normal incident linearly X-polarized plane waves were selected to estimate the interaction between the propagating plane waves and the heterostructures. ZnO was considered as a dielectric material with refractive index $n=2.03$.

2.9. Photocatalysis measurements

The photoinduced degradation of rhodamine B (RhB) or methylene blue (MB) as the test pollutant under UV ($\lambda=254$ nm, UV

source), visible ($\lambda > 420$ nm or $\lambda > 590$ nm, xenon lamp with pass filter), or full-spectrum light irradiation ($\lambda > 200$ nm, xenon lamp) is utilized to investigate the photocatalytic activity of the photocatalysts. For photocatalytic studies, 10 mg samples containing photocatalysts were dispersed in 30 mL of 5 ppm RhB or MB aqueous solution. Prior to irradiation, the photocatalysts were immersed in the RhB or MB solution and kept in the dark for 30 min to establish an adsorption-desorption equilibrium between the dye and the surface of the catalysts. The solutions which contained photocatalysts were subsequently irradiated. The reaction mixtures were exposed to light irradiation (power density ~ 2 mW $^{-1}$ cm 2) under vigorous stirring. The concentration of RhB and MB was determined by the UV-vis absorption of the dye at λ_{max} of 554 nm and 665 nm, respectively.

2.10. Preparation of the single NPs-decorated ZnO nanorod photoconductive device:

The ZNRs were synthesized in the solution using the hydrothermal method as mentioned before. They were placed in a vial containing TA-functionalized AgNPs or AuNPs, which have been dispersed for 1 h for preparation of chemically assembled ZNRs-AgNPs or ZNRs-AuNPs heterostructures. After that, the ZNRs-AgNPs or ZNRs-AuNPs heterostructures in the aqueous solution were transferred to Si-based substrates. The individual ZnO nanorod decorated with AgNPs or AuNPs was subsequently used for the fabrication of the photoconductive device. A full-spectrum light ($\lambda > 200$ nm, xenon lamp) was illuminated on a single NPs-decorated nanorod which was connected to one pair of Pt electrodes deposited by focusing ion beam technique, and the photocurrent was measured using a two-probe method.

3. Results and discussion

3.1. Synthesis of ZNRs-AgNPs and ZNRs-AuNPs Heterostructures Using Bifunctional Linkers

The decoration of metal NPs (Ag or Au) on nanostructured semiconductors has been demonstrated by reducing metal salt precursors directly (e.g., AgNO_3 , HAuCl_4 , and so forth) [19,39–41]. However, aggregation of NPs usually occurred on the supporting substrates, especially at high particles loading, which leads to significantly decrease the metal-support active sites on both the metal and the support which are needed for the photocatalytic simultaneous reduction and oxidation reactions to occur. In addition, other works have reported that the aggregated plasmonic NPs on 2D semiconductors led to the distortion of plasmonic effect, which produced a counter effect of suppressing the photocurrent in the optoelectronic devices [42,43]. Thus, aggregation of NPs on the semiconductors hinders the realization of highly efficient photocatalysts and photovoltaics. To improve the plasmonic NPs-semiconductors interaction, we have prepared a bifunctional TA linker containing the carboxylate groups for ZnO nanorods attachment and thiols as strong AgNPs or AuNPs binding functional groups, as shown in Fig. 1a. Such molecular linker acts as an effective bridge between two materials enabling the preparation of diverse hybrids using different strategies that might affect their plasmonic properties. The TA-functionalized NPs with sufficient steric stabilization perform as “spacer” to prevent the particles from aggregating, even at high NPs loading due to repulsive electrostatic force exerted by the negatively charged TA-functionalized NPs.

Briefly, the AgNPs and AuNPs were synthesized by controlling the concentration ratio of AgNO_3 to NaBH_4 and HAuCl_4 to $\text{Na}_3\text{C}_6\text{H}_5\text{O}_7 \cdot 2\text{H}_2\text{O}$, respectively. After that, the TA molecules were

added to AgNPs or AuNPs solutions, of which basicity was pre-adjusted to pH 11 by 0.5 M NaOH, and left for self-assembling for 48 h. Fig. 1b shows the optical absorption spectra of AgNPs and AuNPs before and after modification with TA. We found that the SPR peaks of the AgNPs and AuNPs both exhibited red-shift from 388 to 398 nm and 516 to 521 nm, respectively. The shift in the position of the SPR peaks, which results from a change in the dielectric property of the environment, suggests the attachment of a layer of adsorbed TA surfactant around the AgNPs or AuNPs by formation of strong S–Ag or S–Au bonds [44]. In comparison with the bare AgNPs and AuNPs, the TA-functionalized AgNPs and AuNPs exhibit different response to pH of solution, as shown in Fig. 1c. After adding HCl solution (10 μl , 1.0 M), the TA-functionalized AgNPs and AuNPs solutions immediately appeared to be of purple and orange color, respectively. This phenomenon suggests particle aggregation [45]. The aggregation can be attributed to the formation of strong intermolecular hydrogen bonding in the presence of the carboxylate-terminated functionalized NPs in the acidic environment. Transmission electron microscopy (TEM) observation reveals the TA-functionalized AgNPs and AuNPs are well dispersed, uniformly sized, and spherical in shape (Fig. 1d and e). The sizes of the TA-functionalized AgNPs and AuNPs were estimated by measuring 100 NPs, indicating that the average size and standard deviation of the TA-functionalized AgNPs and AuNPs are $9.65\text{ nm} \pm 1.42$ and $10.46\text{ nm} \pm 0.76$, respectively.

The ZNRs were synthesized by hydrothermal reaction of $\text{Zn}(\text{NO}_3)_2 \cdot 6\text{H}_2\text{O}$ and $\text{C}_6\text{H}_{12}\text{N}_4$ precursors in an aqueous solution at 90°C for 2 h. Fig. 1f displays field emission scanning electron microscopy (SEM) image of the ZNRs with a well-defined morphology. The high-resolution TEM (HRTEM) and photoluminescence (PL) results indicate that the ZNRs obtained in this investigation possess excellent quality (Supporting information, Figs. S1 and S2). The surface Zn-atom sites of ZnO have a strong affinity for the carboxylate group of the molecular linkers [46]. The carboxylate-rich surfaces of the TA-functionalized AgNPs or AuNPs were exposed to the ZNRs, the particles chemisorbed gradually, forming a monolayer and conformal coating on the surface of the ZNRs, as shown in Fig. 1g and h. Fig. S3 shows the SEM images of the ZNRs-AgNPs and ZNRs-AuNPs heterostructures with AgNPs and AuNPs prepared by the self-assembly method at various AgNPs and AuNPs concentrations of 10, 20, 30, and 60 nM for 1 h. The formation of a monolayer of arranged NPs without aggregation on the ZNRs is commonly observed. We used the inductively-coupled plasma mass spectrometry (ICP-MS) measurements to quantitatively determine the metal loadings, as shown in Fig. S4. Both the Ag and Au content increased linearly with an increase of the TA-functionalized AgNPs and AuNPs concentration within 0–30 nM. By controlling the initial concentration of NPs at 30 nM, the high-density unaggregated NPs were linked molecularly to the entire surface of the ZNRs. Therefore, the maximal NP loading content in the ZNRs-NPs heterostructures can reach approximately 30 wt %. Above 30 nM, the loading content of NPs on ZNRs remained essentially unchanged, revealing that the TA-functionalized NPs possessing sufficient steric stabilization can prevent the particles from aggregating.

Fig. 2a and b shows the corresponding photograph of aqueous dispersions of the bare ZNRs, ZNRs-AgNPs, and ZNRs-AuNPs samples. The heterostructures with an extensive range of Ag or Au loadings resulted in the significant difference in the color of the suspensions. Diffuse reflectance absorption spectra of the bare ZNRs, ZNRs-AgNPs and ZNRs-AuNPs heterostructures with different NPs loading are shown in Fig. 2c. The intense UV absorption band below 400 nm could be assigned to the intrinsic bandgap absorption of the ZnO (band gap 3.31 eV). Compared with the bare ZNRs, the ZNRs-AgNPs and ZNRs-AuNPs heterostructures have much higher absorption in the visible region. It is caused by the SPR of the AgNPs or AuNPs, as expected. As the NPs loading increased,

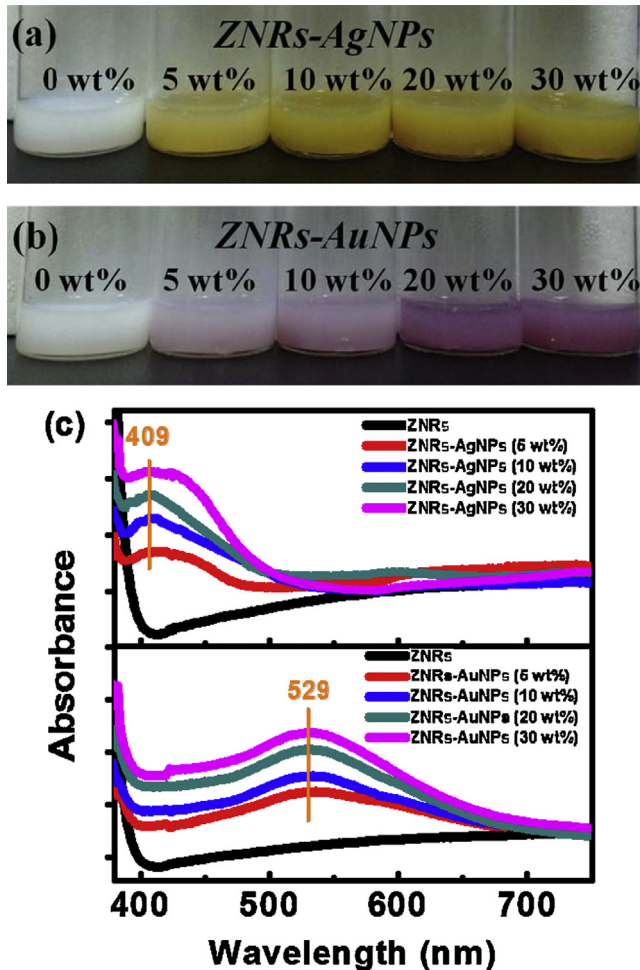


Fig. 2. Photographs of aqueous dispersions of (a) ZNRs-AgNPs and (b) ZNRs-AuNPs samples. (c) Diffuse reflectance absorption spectra of the bare ZNRs, ZNRs-AgNPs and ZNRs-AuNPs heterostructures.

the absorbance that originated in the SPR of AgNPs (at 409 nm) or AuNPs (at 529 nm) considerably increased, suggesting that the NPs loading could be effectively controlled, enabling the conditions of the photocatalytic reaction to be optimized. Note that the maximum resonant wavelength of the ZNRs-AgNPs and ZNRs-AuNPs heterostructures are distinctly red-shifted by approximately 11 nm and 8 nm relative to the TA-functionalized AgNPs and AuNPs, respectively. The observed shifts can be attributed to the close proximity of the TA-functionalized NPs to the ZNRs surface, which can alter the Ag or Au SPR feature because of the change in the dielectric property of the environment [37,44]. It should be emphasized that the size of AgNPs or AuNPs on ZNRs was all preserved after the anchoring process. The described methodology of heterostructure synthesis allows the adjustment of the NPs loading while keeping the same size distribution of NPs. This enables us to investigate only the influence of the NPs loading on photocatalytic properties of the heterostructures as the size is controlled. We have developed a very simple synthetic method to accurately control the loading of the NPs without aggregation onto the surface of nanostructured ZnO in a very wide range (0–30 wt.% for Ag or Au loading). Other methods used in heterostructure synthesis often do not allow the precise control of the NPs size distribution when the NPs loading is changed, therefore introducing too many variable factors that might be responsible for catalytic changes [47,48].

Fig. 3a shows the X-ray diffraction (XRD) spectra of the ZNRs, ZNRs-AgNPs (30 wt.%), and ZNRs-AuNPs (30 wt.%) heterostruc-

tures. All diffraction peaks of the ZNRs can be indexed to the hexagonal wurtzite structures. For the ZNRs-AgNPs and ZNRs-AuNPs heterostructures, the presence of Ag (111) and Au (111) planes in the diffraction spectra confirms the coverage of the AgNPs and AuNPs on the ZNRs, respectively. Fig. 3b displays the S 2p peaks of high-resolution X-ray photoelectron spectroscopy (XPS) of the ZNRs-AgNPs (30 wt.%) and ZNRs-AuNPs (30 wt.%) heterostructures. The S 2p region exhibits the S 2p doublet with binding energies of 160.6–160.7 eV (S 2p_{3/2}) and 162.3–162.4 eV (S 2p_{1/2}), implying the presence of the S–Ag or S–Au covalent bonds [49,50]. The result corresponds to the chemical state of the sulfur in the TA-functionalized AgNPs or AuNPs. Fig. 3c and d presents the typical TEM image and high-angle annular dark field image of the well dispersed AgNPs on the ZnO nanorod (ZNRs-AgNPs (30 wt.%)). Fig. 3e is a magnified TEM image of the side region of a single ZnO nanorod with AgNPs decoration. It is observed that the densely dispersed AgNPs have a uniform size of about 10 nm. A HRTEM image (Fig. 3f) from the square area in Fig. 3e reveals an atomic plane spacing of 0.23 nm corresponding to the (111) plane of polycrystalline Ag. EDX elemental mappings of the ZNRs-AgNPs (Ag, S, Zn, and O) heterostructures from TEM analysis are shown in Fig. 3g, respectively. The similar TEM results of the ZNRs-AuNPs (30 wt.%) heterostructures are also seen in Fig. S5. Accordingly, these results further confirm that the TA-functionalized NPs distribute uniformly on the surface of the one dimensional ZnO nanostructures.

3.2. Photocatalytic Activities of ZNRs-AgNPs and ZNRs-AuNPs Heterostructures

The photocatalytic degradation of organic pollutant is of great significance in environmental purification and represents a commonly used approach to characterize the catalytic performance of photocatalysts [11,12,15,16,30]. To this end, in the present study the photoinduced decomposition of rhodamine B (RhB) as the test pollutant under UV ($\lambda = 254$ nm), visible ($\lambda > 420$ nm or $\lambda > 590$ nm), or full-spectrum light irradiation ($\lambda > 200$ nm) with power density of ~ 2 mW⁻¹ cm² are utilized to evaluate the photoconversion efficiency of the samples. The photocatalytic activities of the ZNRs, ZNRs-AgNPs, and ZNRs-AuNPs under different light irradiations are obtained in Fig. 4. The catalytic kinetics of heterogeneous photocatalysis can be analyzed using the Langmuir–Hinshelwood model with first-order kinetics [51]:

$$\ln \left(\frac{C_0}{C} \right) = k_a t \quad (1)$$

where C_0 and C are the concentrations of the RhB before and after light irradiation, respectively. The photocatalytic degradation can be quantitatively evaluated by the reaction rate constant (k_a), which can be obtained from the plots of $\ln(C_0/C)$ versus irradiation time (t). For example, Fig. S6 shows the $\ln(C_0/C)$ versus irradiation time curves of the RhB photodegradation using the ZNRs, ZNRs-AgNPs (30 wt.%), and ZNRs-AuNPs (30 wt.%) photocatalysts under full-spectrum light irradiation. The curves shown in Fig. S6 are nearly linear, which indicates that the kinetic data of the RhB photodegradation fit well to the first-order reaction model. The (blank) RhB without catalysts showed immeasurable photolysis. Additionally, the control experiments for the photocatalytic measurements of the mixed AgNPs (30 nM) or AuNPs (30 nM) and ZNRs (10 mg) without using bifunctional TA linkers were performed, as shown in Fig. S6. In comparison with the ZNRs-AgNPs (30 wt.%) or ZNRs-AuNPs (30 wt.%) heterostructures using the TA linkers, samples without using TA linkers exhibited considerably low photocatalytic reaction rates under full-spectrum light irradiation. This result clearly indicated that the uniform distribution of the AgNPs or AuNPs linked molecularly to the entire surface of the ZNRs to

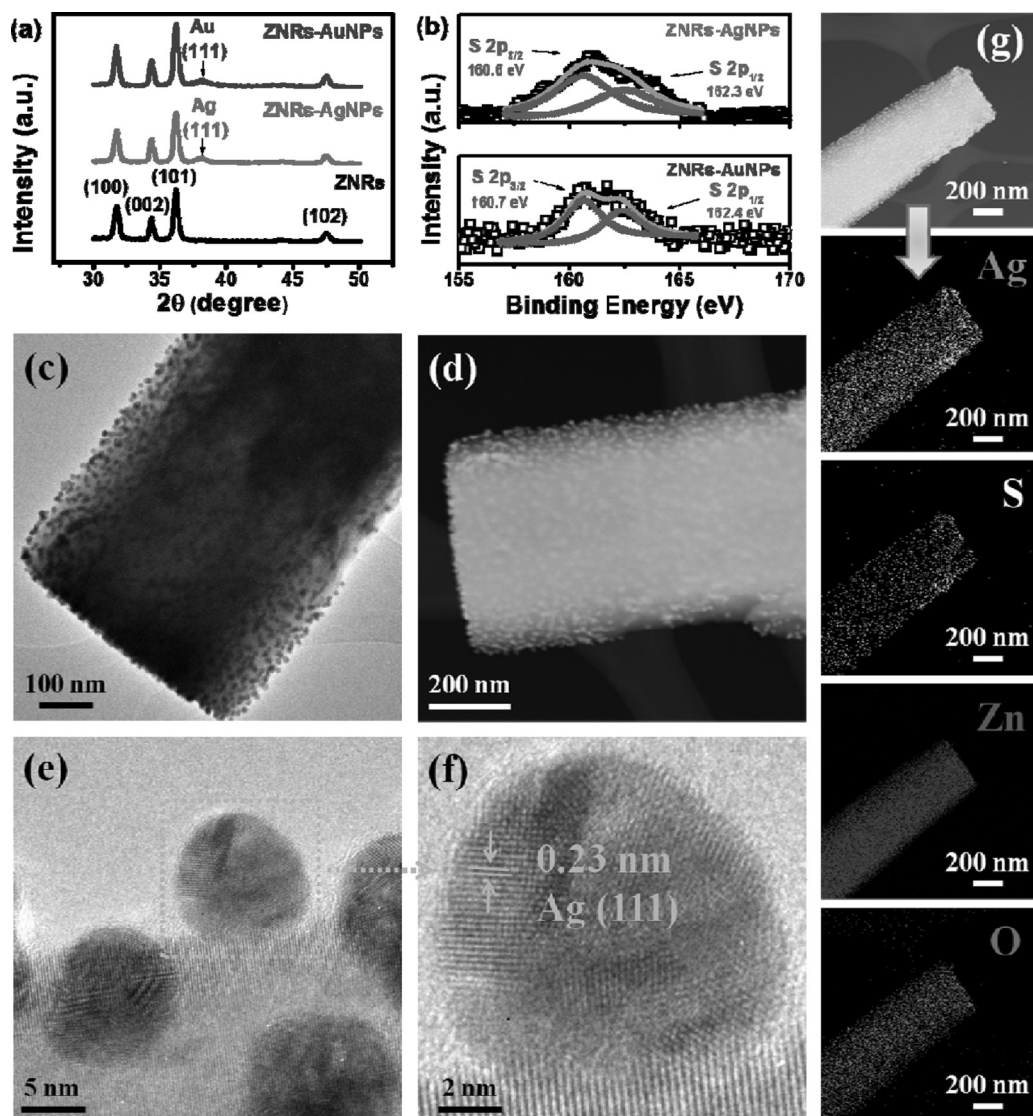


Fig. 3. (a) XRD spectra of the samples. (b) The S 2p region of the XPS spectra of ZNRs-AgNPs and ZNRs-AuNPs heterostructures. (c)–(f) TEM analysis of ZNRs-AgNPs heterostructures. (g) EDX elemental mappings of ZNRs-AgNPs.

form the hybrid nanostructures played a positive role on the photocatalytic activity.

Under UV irradiation, the ZNRs-AgNPs and ZNRs-AuNPs photocatalysts both show a proportional increase in photocatalytic reaction rate with increasing NPs loading content (Fig. 4a). In our study, the SPR peaks of the AgNPs and AuNPs on the ZNRs were observed at 409 nm and 529 nm (Fig. 2), respectively. Therefore, there is no plasmonic effect induced by the ZNRs-AgNPs or ZNRs-AuNPs under UV light irradiation since the frequency of UV light could not match the frequency of the surface electrons of the AgNPs or AuNPs. It is well known that the metal NPs deposited on semiconductor retards the electron–hole recombination by serving as an electron sink(electron trapping) [52–54]. With increasing NPs loading, more photoinduced electrons will transfer from the conduction band of the ZNRs to the NPs as driven by the energy difference, which improves the separation of the photoexcited electron–hole pairs, increases the surface area for the photocatalytic reactions, and consequently enhances the photoactivity for decomposition of RhB compounds. In the earlier reports, the decrease of the photoconversion efficiency for higher metal NPs loadings was observed in ZnO-NPs or TiO₂-NPs composites [39,55,56], which is directly connected to the merging of metal

agglomerates with the formation of the continuous metal film. It hinders the metal-support active sites, on both the metal and the support, which are needed for the photochemical reaction to occur. In our cases, 10 nm AgNPs or AuNPs without aggregation have been uniformly dispersed on the surface of the ZNRs even at maximal NPs loading. The ZNRs-NPs photocatalysts proposed in this work thus exhibit superior photoactivity without causing any negative effect in the photochemical reactions. It must be emphasized that the ZNRs-AuNPs deliver a RhB degradation rate higher than the ZNRs-AgNPs with the same particle loading under UV irradiation. This result can be attributed to the positioning of the AuNPs on the surface of the ZNRs which shifts the apparent Fermi level of the composite to the more negative values than that of the AgNPs, which enables the AuNPs to act as more efficient electron sinks for the storage of photogenerated electrons and to make the catalytic system more reductive [55–57]. It therefore increases the rate of RhB degradation under UV irradiation. To confirm the analytical results discussed above, the charge separation efficiency of the bare ZNRs, ZNRs-AgNPs (30 wt.%), and ZNRs-AuNPs (30 wt.%) was investigated by PL spectra with an excitation wavelength of 325 nm, as shown in Fig. S7. The main emission peak is centered at about 374 nm in each spectrum, in which the luminescence

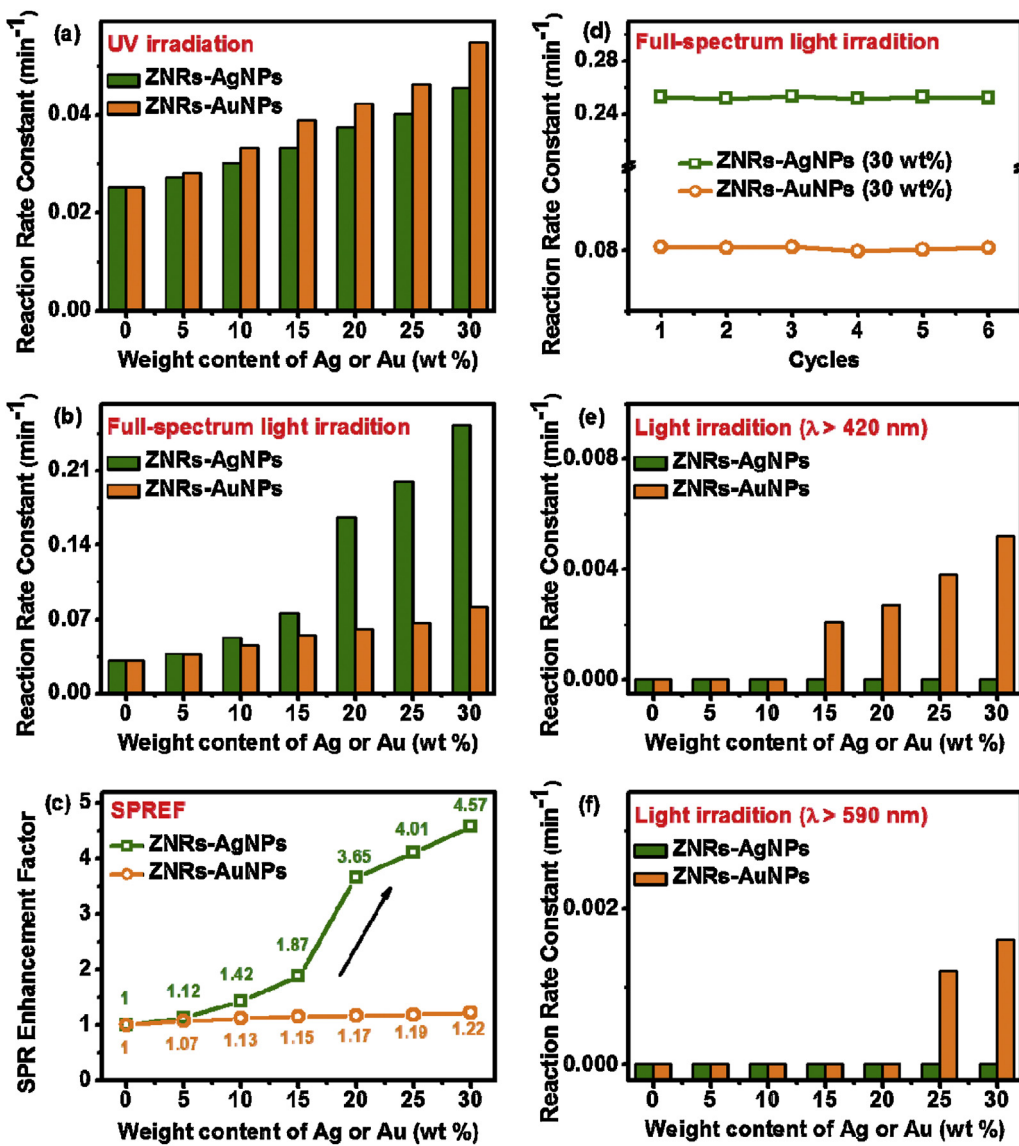


Fig. 4. Photocatalytic reaction rates of the photocatalysts under (a) UV (b) full-spectrum light irradiation. (c) SPREF of ZNRs-AgNPs and ZNRs-AuNPs photocatalysts. (d) Cyclic photodegradation of RhB using ZNRs-AgNPs and ZNRs-AuNPs photocatalysts. Photocatalytic reaction rates of the photocatalysts under (e) $\lambda > 420$ nm and (f) $\lambda > 590$ nm light irradiation.

corresponds to the ZnO band gap recombination of electron–hole pairs. PL emission originated from the recombination of excited electrons and holes so that the intensity of the PL spectrum indicates the charge recombination rate. Fig. S7 shows that the bare ZNRs sample exhibits the strongest intensity of PL emission, confirming the fastest charge recombination rate of the bare ZNRs sample among all investigated photocatalysts. Importantly, the ZNRs-AuNPs (30 wt.%) heterostructure exhibited the lowest recombination rate of the excited electrons and holes, as indicated by the weakest PL emission (at 374 nm). Hence, the result in Fig. S7 proves that the ZNRs-AuNPs (30 wt.%) heterostructure can inhibit the charge recombination between photoinduced electron–hole pairs better than that of the ZNRs-AgNPs (30 wt.%) heterostructure. It is consistent with the discussion on the charge carrier separation and photocatalytic experimental data (Fig. 4a) in this study.

As it can be seen in Fig. 4b, the promotion effect of the AgNPs or AuNPs on the photoactivity of the ZNRs under full-spectrum light irradiation is significantly higher than that under UV irradiation. It could be attributed to the localized SPR effects of the plasmonic NPs. In addition, the ZNRs-AgNPs samples show high photocat-

alytic activity under full-spectrum light irradiation, exceeding the corresponding ZNRs-AuNPs samples. The ZNRs-AgNPs (30 wt.%) exhibits a photoreaction rate ~ 3.1 times higher than that recorded for the ZNRs-AuNPs (30 wt.%) under full-spectrum light illumination. According to the photocatalytic results (Fig. 4), the loading of the plasmonic NPs on the ZNRs can enhance the photocatalytic performances, which could be attributed to the cocatalyst effect (charge separation and SPR effects). Furthermore, we define a SPR enhancement factor (SPREF), which can clearly reveal the plasmonic effect on the photocatalytic promotion excluding UV light induced improvement of charge separation in the ZNRs-NPs heterostructures, as follows:

$$\text{SPREF} = \frac{k_{\text{full-spectrum(ZNRs-NPs)}}/k_{\text{full-spectrum(ZNRs)}}}{k_{\text{UV(ZNRs-NPs)}}/k_{\text{UV(ZNRs)}}} \quad (2)$$

where $k_{\text{full-spectrum}}$ and k_{UV} are photocatalytic reaction rate constants under full-spectrum and UV light irradiation, respectively. The calculated SPREF of the ZNRs-AgNPs and ZNRs-AuNPs photocatalysts are summarized in Fig. 4c. The SPREF of the ZNRs-AgNPs and ZNRs-AuNPs are higher than 1 and increase with the NPs con-

tent. It is due to the contribution of SPR effect induced enhancement of photocatalytic activity.

The robustness of the ZNRs-NPs photocatalysts was confirmed by repeated photocatalytic experiments using a recycled catalyst sample under the same reaction conditions. As shown in Fig. 4d, the photocatalysts maintain relatively steady photocatalytic activity. Fig. S8 displays the SEM images of the ZNRs-AgNPs and ZNRs-AuNPs photocatalysts after 6 catalytic cycles, indicating that the morphologies are unchanged after 6 cycles of reuse. The stability of the TA molecules after photocatalysis was investigated by Fourier-transform infrared (FTIR) spectroscopy and XPS, as shown in Figs. S9 and S10. The chemical bonding of sulfur of the ZNRs-NPs heterostructures after 6 photocatalytic cycles is also almost the same as that of the freshly prepared heterostructures. These results reveal that the photocatalysts demonstrated in this study exhibit superior stability under full-spectrum light irradiation. In order to further confirm the performance of the ZNRs-AgNPs and ZNRs-AuNPs photocatalysts, their photocatalytic properties for methylene blue (MB) degradation are also conducted under full-spectrum light irradiation. Of note, as depicted in Fig. S11, the experimental results for the MB degradation are fairly consistent with the above results for the RhB degradation. Moreover, according to the XPS and photocatalytic analysis (Supporting information, Figs. S12–S15), we confirm that that the TA molecular linkers in the ZNRs-NPs samples would not cause the poisoning effect of the photocatalytic activities.

In order to study the plasmonic enhanced mechanism, we have performed the action spectral analysis on the plasmonic effects by means of incident photon-to-current conversion efficiency (IPCE) which exhibited a clear wavelength dependence of the photocurrent enhancement. Fig. S16 shows the IPCE curves of the bare ZNRs, ZNRs-AgNPs (30 wt.%), and ZNRs-AuNPs (30 wt.%). The ZNRs-AgNPs (30 wt.%) and ZNRs-AuNPs (30 wt.%) both exhibited improved photoactivity compared with the bare ZNRs in the UV region, which suggests that the AgNPs or AuNPs on the ZnO semiconductors improves the charge carrier separation, and consequently enhances the photocurrent in the UV region. It is consistent with its photocatalytic enhancement observed under UV light irradiation (Fig. 4a) and PL results (Fig. S7). Clearly, for the ZNRs-AgNPs (30 wt.%), an observable shoulder at around 400–410 nm was present and a substantial photoactivity in the visible light region from 400 to 500 nm. Additionally, the ZNRs-AuNPs (30 wt.%) have obvious IPCE peak centered at 520 nm. The results are well-matched with the corresponding AgNPs and AuNPs SPR absorption peaks in the visible region (Fig. 2c). This SPR wavelength-dependent IPCE feature signifies that the plasmonic effect of the AgNPs or AuNPs is responsible for the improved photoactivity of the ZNRs-NPs samples. Several possible mechanisms may contribute to the enhanced photoconversion efficiency in a plasmonic-photocatalyst system involving: (1) scattering and anti-reflection effects [2,37]; (2) plasmon-induced heating [58]; (3) plasmon-induced hot electron–hole pairs (hot electron transfer) [15,18,27]; and (4) electromagnetic field mechanism [14,17,21,22,25,28,30]. First, we can exclude scattering and anti-reflection mechanisms for the 10 nm-sized plasmonic NPs decorated ZNRs in our cases, because it normally occurs in metals with particle sizes larger than 100 nm in diameter [2,37]. In order to ensure that the enhanced photocatalytic activity was not caused by plasmon-induced heating in the NPs, the degradation of RhB was tested under full-spectrum light irradiation in the presence of the bare AgNPs or AuNPs, as shown in Fig. S17. Both AgNPs and AuNPs were unable to thermally activate the degradation of RhB under light irradiation. The plasmon-induced heating effect thus can be ruled out for the present ZNRs-NPs systems. Several groups have confirmed that hot electron transfer mechanism should be the contributor to the enhanced photocatalytic performance of the plasmonic metal-semiconductor heterostructures under visible light illumination [15,18,27]. This previously

proposed model treats the plasmon excitation as similar in nature to an electron–hole pair. As shown in Fig. 4e and f, the visible light photocatalytic activity ($\lambda > 420$ nm or $\lambda > 590$ nm) caused by the SPR effect of Au is insignificant compared to the full-spectrum light activity for the ZNRs-AuNPs samples. This clearly indicates that hot electron transfer mechanism is not the major contributor to the improved photoactivity for the ZNRs-AuNPs samples. Due to the spectrum overlap of the AgNPs SPR and the ZNRs absorption, it is critical to distinguish the photocatalytic activity of the SPR induced effect from that of the excited ZnO semiconductor. However, since the conduction band energy of the ZnO is higher than the Fermi energy of Ag, the direct transfer of plasmon-induced hot electrons from Ag to ZnO is energetically unfavorable [21,57].

The photocatalytic enhancement observed under light illumination can be understood by simulating the electromagnetic response of the ZNRs-AgNPs and ZNRs-AuNPs photocatalysts using the 3D FDTD method. The electromagnetic fields affected by ZnO-NPs immersed in water with refractive index $n = 1.333$ simulated by 3D FDTD under 410 or 530 nm monochromatic light illuminations are illustrated in Fig. 5a. We simulated the electromagnetic field distributions of coupled 10 nm sized AgNPs or AuNPs which are coated on ZnO surfaces with 5, 10, 15, and 20 nm interparticle gaps. In the simulation, the normal incident linearly X-polarized plane waves with wavelength 410 and 530 nm were selected to estimate the interaction between the propagating plane waves and the heterostructures. The selected wavelengths were in close proximity to the plasmonic peak positions of the AgNPs (410 nm) and AuNPs (530 nm) according to the UV-vis spectra (Fig. 2c). Simulation results clearly confirm the presence of localized SPR enhanced electromagnetic field for the ZNRs-AgNPs and ZNRs-AuNPs photocatalysts. The SPR of the plasmonic metallic NPs can be described as the resonant photon-induced collective oscillation of valence electrons, established when the frequency of photons matches the natural frequency of surface electrons oscillating against the restoring force of positive nuclei [37]. Therefore, the resonant photon wavelength is different for different metals. In our work, the SPR peaks of the AgNPs and AuNPs on the ZNRs were observed at 409 nm and 529 nm (Fig. 2), respectively. The AgNPs support the formation of the SPRs in response to higher energy light flux and localize higher electromagnetic energy to their surfaces than that of the AuNPs. Therefore, the ZNRs-AgNPs are found to produce high intensity of electromagnetic field, which explains the high enhancement of photocatalytic activity of the ZNRs-AgNPs than the ZNRs-AuNPs under full-spectrum light irradiation, as shown in Fig. 4b. The electromagnetic field mechanism is based on the interaction of the semiconductor with the strong SPR-induced electromagnetic fields located nearby the plasmonic nanostructures. The enhanced electromagnetic field improves the light absorption of ZnO and facilitates the selective formation of electron–hole pairs in the near-surface region of the neighboring semiconductor, which has gained acceptance [21]. As the generation rate of electron–hole pairs in a semiconductor is proportional to the local intensity of the electric field (more specifically $|E|^2$), the generation rate of electron–hole pairs in the semiconductor increases by a few orders of magnitude. It means that the probability of photoreaction can be enhanced effectively.

Most importantly, in high AgNPs loading region, the obtained SPREF of the ZNRs-AgNPs photocatalysts significantly increase with Ag content. Regarding this result, we have determined the average gap distance between the NPs (edge to edge separation) of the ZNRs-NPs heterostructures with the various NPs loading content. Figs. S18 and S19 show the high-magnification SEM images and corresponding histograms representing the interparticle spacing distribution of the ZNRs-AgNPs and ZNRs-AuNPs heterostructures at the various AgNPs and AuNPs of 5, 10, 20, and 30 wt.%, respectively. The calculated mean and the corresponding standard

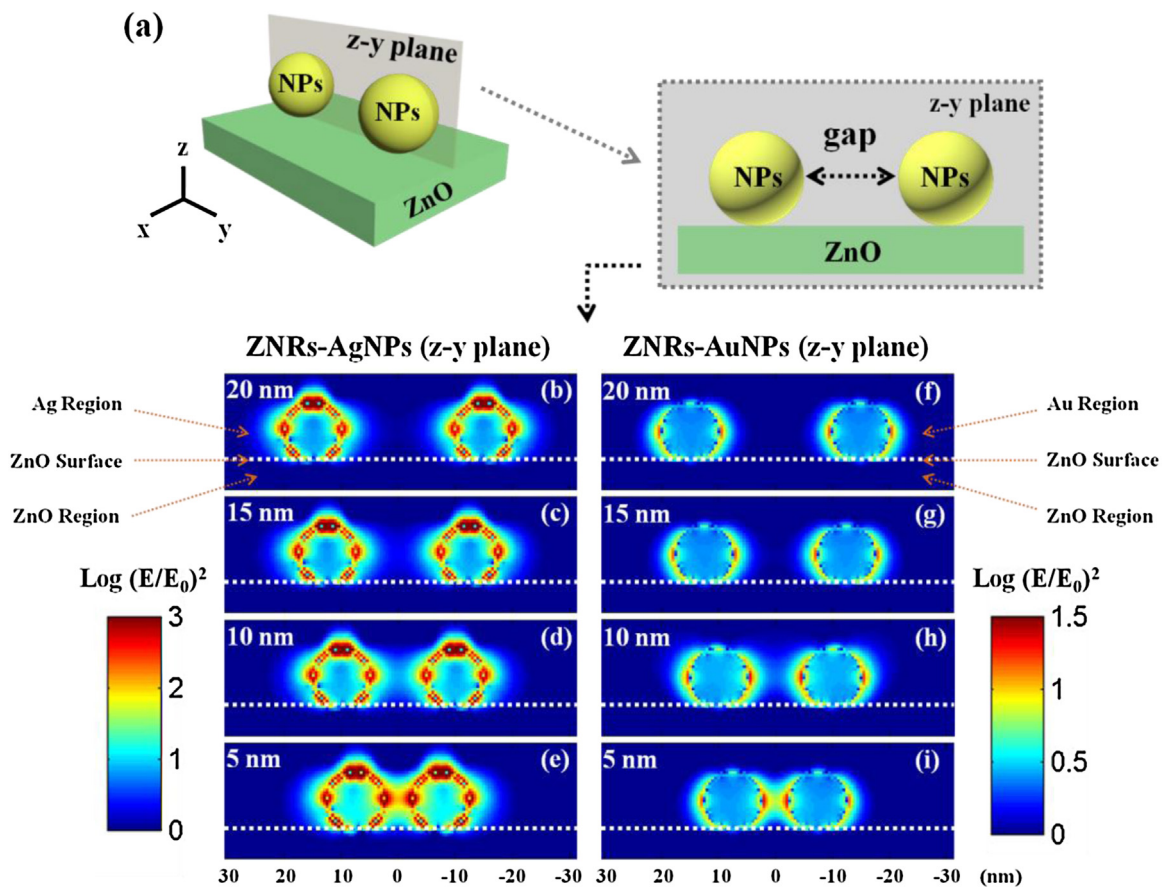


Fig. 5. (a) The simulation model of the 3D FDTD simulation of the ZNRs-NPs heterostructures. Electromagnetic field distributions (z-y plane) of coupled 10 nm sized (b–e) AgNPs and (f–i) AuNPs which are coated on ZnO surfaces with 20, 15, 10, and 5 nm interparticle gaps.

deviation of the interparticle spacing are summarized in Table 1. It clearly indicates that the increase of the NPs content in the ZNRs-NPs heterostructures results in a decrease in the interparticle spacing simultaneously. The possible mechanism to decrease the interparticle spacing as increasing the NPs coverage on the ZNRs by controlling the initial concentration of the TA-functionalized AgNPs or AuNPs in the reaction is depicted in Fig. S20. When the low concentration of the carboxylate-rich surfaces of the TA-functionalized NPs were exposed to the ZNRs, for example 5 and 10 nM, the small amount of the NPs were distributed on the surface of the ZNRs. It results in the larger gap distance between the NPs. With a further increase in the concentration of the TA-functionalized NPs to 20 or 30 nM, the ZNRs were successfully decorated by many uniformly dispersed NPs, leading to the small interparticle gaps (<10 nm). The SEM images of the ZNRs-NPs (20 wt.%) and ZNRs-NPs (30 wt.%) revealed that the average distances between NPs are approximately 9.1–9.7 and 6.2–7.1 nm, respectively. Fig. 5d represents the electromagnetic coupling effect between the AgNPs with

a 10 nm interparticle gap. The plasmon coupling effect is responsible for the high electromagnetic field intensity in the gap between the coupled AgNPs. When a plasmonic particle is placed in close proximity to one another, much higher localized electromagnetic fields than that for a single particle are generated in the interparticle gap, called “hot spot” [3,21,33–37]. When the interparticle spacing decreases to 5 nm, the electromagnetic response of the ZNRs-AgNPs (as shown in Fig. 5e) is dominated by local “hot spot” which can be observed between the coupled AgNPs around the ZnO surfaces. In the case of the AuNPs, the electromagnetic field intensity due to the plasmon coupling effect (hot spot region) is comparatively weak.

We further calculated the electromagnetic field enhancement as a function of distance from the surface of the NPs alone line a and b (Fig. S21, schematic diagram) for the ZNRs-AgNPs and ZNRs-AuNPs samples, as shown in Fig. 6. Most importantly, for the AgNPs coated on ZnO surfaces with a 5 nm gap, the stronger plasmon coupling effect between the AgNPs (line a) results in significant increases of the electromagnetic field inside the ZnO, as shown in Fig. 6a. The corresponding maximal electromagnetic field enhancement is 8-fold around the local hot spots near the surface of the ZnO. The enhancement quickly decays to a much smaller value of 1 at a distance of 5 nm from the local hot spots. In addition, the electromagnetic field enhancement, as a function of distance alone line b from the surface of the AgNPs with a 5 nm gap, is also higher than that of the coupled AgNPs with larger interparticle spacing, as shown in Fig. 6b. The localized electromagnetic fields are strengthened by decreasing the interparticle spacing of coupled AgNPs, as described above. In addition, as depicted by FDTD simulations, the plasmon coupling effect of AgNPs is more significant than that of coupled AuNPs, as shown in Fig. 6. There-

Table 1

The calculated mean and the corresponding standard deviation of the interparticle spacing.

Samples	AverageDistance (nm)	Samples	AverageDistance (nm)
ZNRs-AgNPs (5 wt.%)	59.3 ± 30.4	ZNRs-AuNPs (5 wt.%)	54.9 ± 29.2
ZNRs-AgNPs (10 wt.%)	27.8 ± 14.2	ZNRs-AgNPs (10 wt.%)	29.5 ± 13.9
ZNRs-AgNPs (20 wt.%)	9.7 ± 4.9	ZNRs-AuNPs (20 wt.%)	9.1 ± 4.8
ZNRs-AgNPs (30 wt.%)	7.1 ± 4.2	ZNRs-AuNPs (30 wt.%)	6.2 ± 4.0

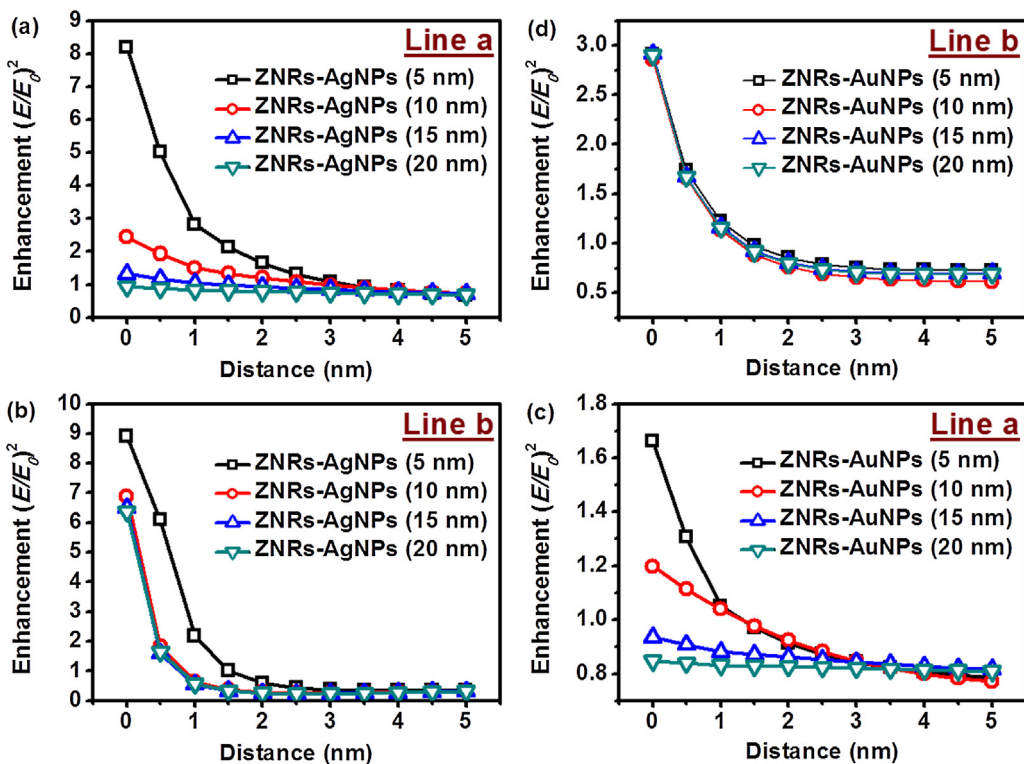


Fig. 6. The electromagnetic field enhancement as a function of distance from the surface of AgNPs along line (a) and (b) for ZNRs-AgNPs heterostructures. The electromagnetic field enhancement as a function of distance from the surface of AuNPs along line (c) a and (d) b for ZNRs-AuNPs heterostructures.

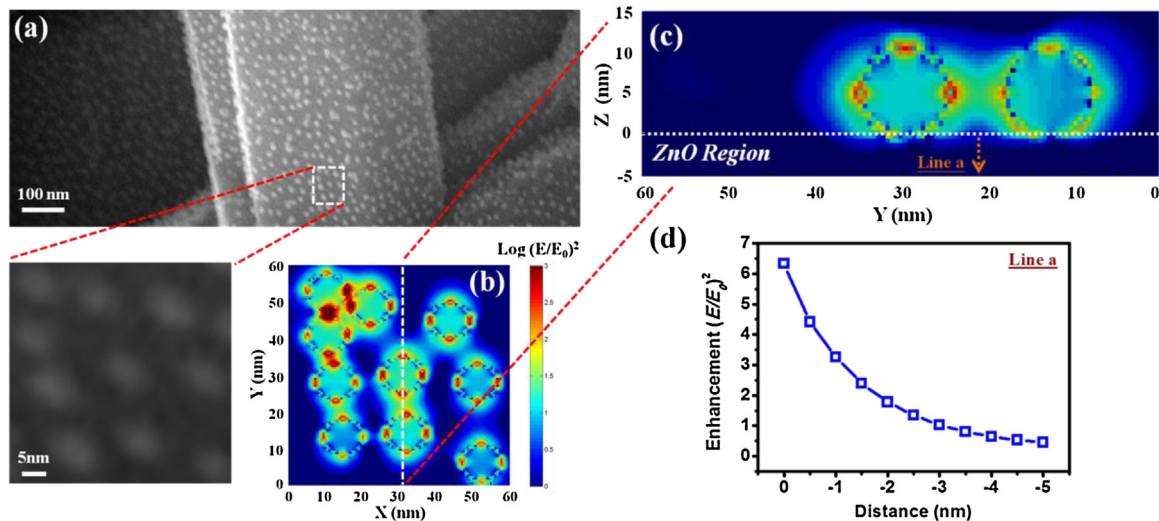


Fig. 7. (a) SEM image and (b) Electromagnetic field distribution on the x-y plane of ZNRs-AgNPs heterostructures. (c) The cross-sectional plot of the electromagnetic field distribution (y-z plane) along the white dashed line in (b). (d) The electromagnetic field enhancement as a function of distance from the surface of ZnO alone line a in (c).

fore, the superior photocatalytic properties achieved in this study can be attributed mainly to the localized electromagnetic field enhancement of the neighboring ZnO by the SPR effect of the AgNPs. Especially, the hot spot resulting from the coupling effect of the neighboring AgNPs magnifies the localized electromagnetic fields exponentially. It also explains that the observed photoreaction rate increases non-linearly with the Ag content under full-spectrum light irradiation.

Furthermore, we have constructed the exact 3D electromagnetic simulation model based on the morphologies of the ZNRs-AgNPs heterostructures from SEM image, as shown in Fig. 7. Fig. 7a shows a SEM image of the ZNRs-AgNPs (30 wt.%) heterostructures, which

reveals the well dispersed AgNPs on the ZNRs. The electromagnetic simulation cell is constructed in Fig. 7b based on the morphologies of the ZNRs-AgNPs heterostructures from the square area of SEM image in Fig. 7a. The local electromagnetic fields of the AgNPs on the ZNRs, as shown in Fig. 7b, are significantly enhanced by plasmonic hot spots at the gap between the close AgNPs under 410 nm light illumination. The importance of the intense local electromagnetic fields can be seen in Fig. 7c, which displays a cross-sectional plot of the electromagnetic field distribution of one of these hot spot regions in the z-dimension. In this hot spot region, we further calculated the electromagnetic field enhancement as a function of distance from the surface of the ZnO alone line a, which indicates

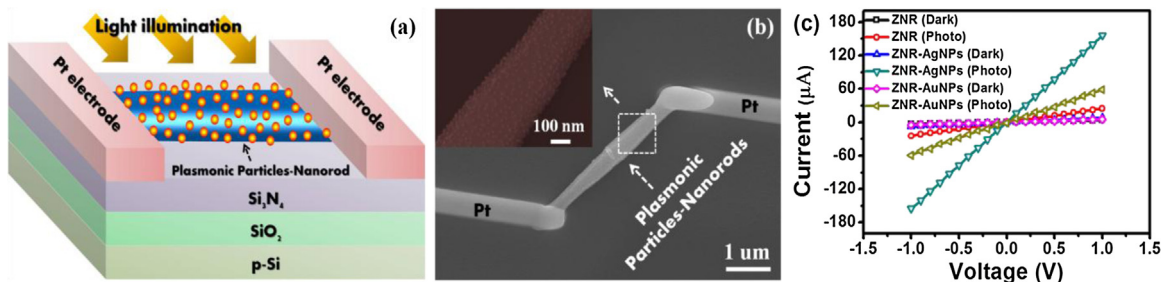


Fig. 8. (a) Schematic of a photoconductive device for the I–V measurements on an individual ZnO nanorod with NPs decoration. (b) SEM image of the photoconductive device. The inset is a high-magnification SEM image of the uniform distribution of AgNPs on ZnO nanorod surface. (c) Photocurrent and dark current of the samples.

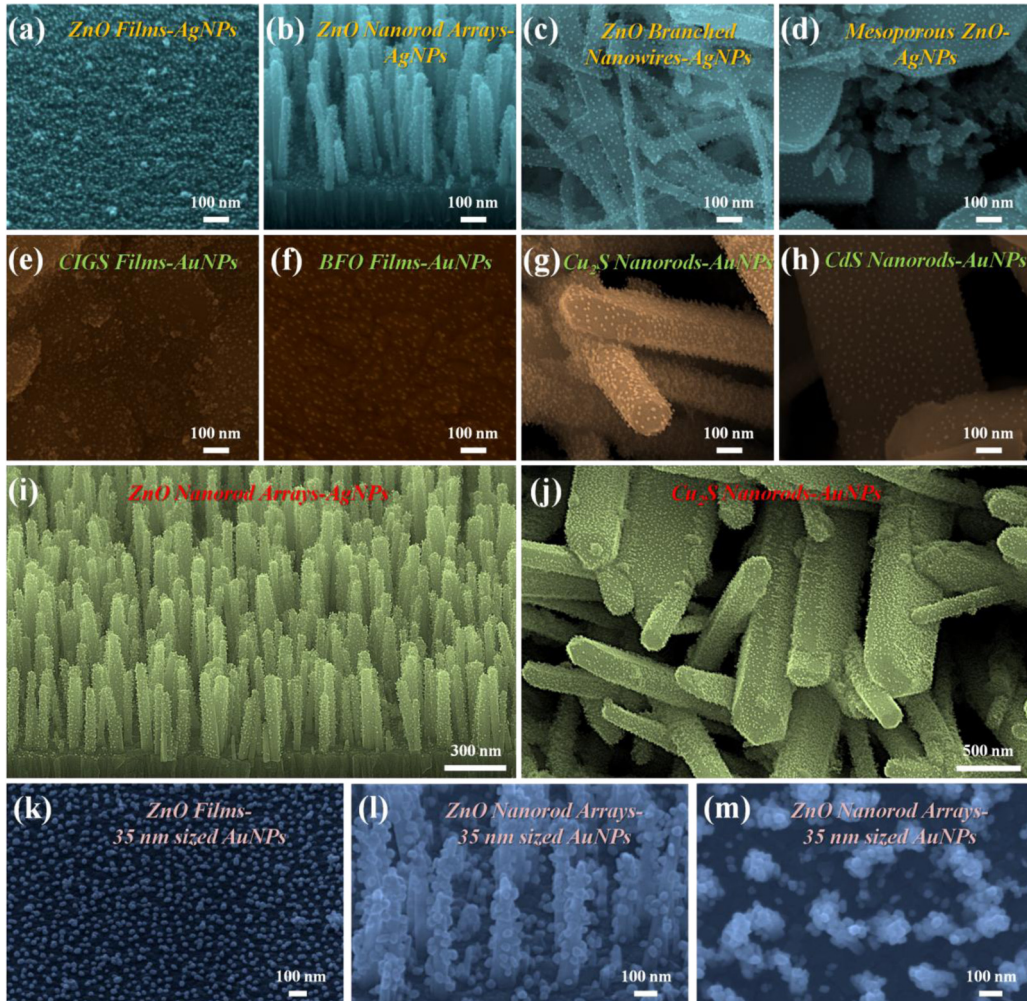


Fig. 9. SEM images of AgNPs on ZnO (a) film, (b) nanorod arrays, (c) branched nanowires, and (d) mesoporous structures. SEM images of AuNPs on (e) CIGS, (f) BFO, (g) Cu₂S, and (h) CdS. Low-magnification SEM images of (i) ZnO nanorod arrays-AgNPs and (j) Cu₂S nanorods-AuNPs heterostructures. (k) SEM image of ZnO film-35 nm sized AuNPs heterostructures. (l) Tilt-angle and top-view (m) SEM images of ZnO nanorod arrays-35 nm sized AuNPs heterostructures.

the electromagnetic field coupling between the AgNPs leads to an electromagnetic field enhancement inside the ZnO, as shown in Fig. 7d. It is consistent with the simulated results in Fig. 5. The more exact electromagnetic field simulation cell which is similar to the morphologies of the heterostructures in Fig. 7 reveals the formation of numerous plasmonic hot spots with high electromagnetic field. The calculated electromagnetic field enhancement as a function of interparticle gap in Fig. 5 is helpful to systematically evaluate the electromagnetic field intensity at different NPs gaps and to realize how interparticle gap will induce the strong plasmonic hot spot effect. Even though the statistical interparticle gap distribution is a normal distribution (Fig. S18), the observed probability of

formed plasmonic hot spots (interparticle gap <10 nm) drastically increases with the increasing Ag content for the ZNRs-AgNPs samples. For example, a statistical fraction of the interparticle gap less than 10 nm for the ZNRs-AgNPs (30 wt.%) is about 90%. In comparison with the ZNRs-AgNPs (10 wt.%), the fraction of the interparticle gap less than 10 nm is about 20%. According to the above simulations, we have confirmed that, when the interparticle spacing decreases to less than 10 nm for the ZNRs-AgNPs heterostructure, the stronger plasmon coupling effect (hot spot effect) between AgNPs results in significant increase of electromagnetic fields. Therefore, we accordingly believe that the successfully fabricated the ZNRs-AgNPs (30 wt.%) heterostructures with the small interpar-

ticle gaps have high number density of plasmonic hot spots with high electromagnetic field. It must be emphasized that the above results give one successful example to synthesize high-density unaggregated plasmonic NPs onto nanostructured semiconductors to generate numerous plasmonic hot spots, which can boost the catalytic activities of the plasmonic coupling photocatalysts.

3.3. Photoconductive Characteristics of Single ZnO Nanorod Decorated with Plasmonic NPs

In order to further understand the interaction between the plasmonic NPs and the ZnO materials, the photocurrent of a single ZnO nanorod with AgNPs or AuNPs decoration was recorded by a current-voltage (I-V) measurement system under full-spectrum light irradiation. A bare ZnO nanorod was used for comparison. The schematic of the photoconductive device for the I-V measurements on a single NPs-decorated nanorod is shown in Fig. 8a. A full-spectrum light was illuminated on the nanorod which was connected to one pair of Pt electrodes deposited by focusing ion beam technique, and the photocurrent was measured using a two-probe method. Fig. 8b is a representative SEM image of the plasmonic AgNPs-decorated ZnO nanorod photoconductive device. The high-magnification SEM image in the inset of Fig. 8b reveals the uniform distribution of the 10 nm sized AgNPs on the single ZnO nanorod surface.

Photocurrent and dark current of the samples are shown in Fig. 8c. For the bare ZnO nanorod, a photoexcited current of 24.8 μ A was recorded at a bias of 1.0 V, whereas high photocurrent of 155.6 and 57.7 μ A for the AgNPs- and AuNPs-decorated ZnO nanorods were achieved at the same bias voltage, respectively. The dark current for the bare and the NPs decorated samples remains invariable. The photocurrent improvement ratio of the AgNPs- and AuNPs-decorated ZnO nanorod, as compared with the bare ZnO nanorod, was about 6.3 and 2.3 fold, respectively. It agrees well with the photocatalytic improvement ratio observed under full-spectrum light irradiation, as shown in Fig. 4b. It can be elucidated according to the above FDTD simulation, the enhancement is caused by localized SPR enhanced local electromagnetic field for the plasmonic NPs-decorated samples.

3.4. Synthesis of heterostructures based on Plasmonic NPs and Diverse Nanostructures or Functional Materials

One of the unique features of the synthesis methodology developed in this study is its excellent scalability. Using the bifunctional TA bridging linkers, heterostructures derived from plasmonic AgNPs on various ZnO nanostructures grown on solid substrates including films, nanorod arrays, branched nanowires, and mesoporous structures, are successfully prepared, as shown in Fig. 9a-d. The ZnO nanostructures-containing substrates with diversely unique morphologies were placed in a vial containing TA-functionalized AgNPs, which have been dispersed for 1 h. The produced heterostructures were then washed with distilled water to remove excess TA-functionalized AgNPs. It resulted in high-density AgNPs on various ZnO nanostructures/substrates.

In addition, the carboxylate-terminated functionalized NPs were stably anchored on a diverse range of functional materials with varied surface properties. The hybrid structures with plasmonic AuNPs and functional materials including CuInGaSe₂ (CIGS) absorber layers [59], multiferroic BiFeO₃ (BFO) films [60], visible-light photoactive Cu₂S [61] and CdS [62] nanorods could be fully constructed by the present chemical assembly method, as shown in Fig. 9e-h. The representative low-magnification SEM images of the ZnO nanorod arrays-AgNPs and Cu₂S-AuNPs nanorods are observed in Fig. 9i and j, respectively. These results demonstrate that high-quality hybrid structures can be synthesized in large

scale. Moreover, the size of plasmonic NPs on semiconductors, which is an important factor for improving the photocatalytic activities, can also be easily controlled. For example, the 35 nm sized TA-functionalized AuNPs were synthesized by controlling the ratio of HAuCl₄ to Na₃C₆H₅O₇·2H₂O concentrations. Fig. 9k-m reveal that the 35 nm sized TA-functionalized AuNPs distribute uniformly on the surface of the ZnO films or nanorod arrays. The flexible synthesis could simplify the synthesis of plasmonic heterostructures and optimize their properties.

4. Conclusions

We successfully synthesized closely dispersed plasmonic NPs onto nanostructured semiconductors for 3D densely organized particles with small interparticle gaps to produce plasmonic hot spots. The hence constructed plasmonic metal-semiconductor 3D heterostructures have high number density of plasmonic hot spots with high electromagnetic field, which can boost the photocatalytic activity. As depicted by 3D FDTD simulations, in the case of densely dispersed AgNPs on ZNRs, the stronger hot spot effect between AgNPs results in significant increase of electromagnetic field inside the ZNRs. Consequently, the ZNRs-AgNPs heterostructures exhibit an 8.26-fold enhanced photocatalytic reaction rate under full-spectrum light illumination in comparison with the bare ZNRs. Moreover, hybrid structures based on the plasmonic NPs on various nanostructures or functional materials were successfully prepared. We envisage that our approach will be potentially useful for creating highly efficient plasmonic-coupled heterostructures in various areas, particularly in the conversion of solar to chemical or electrical energy applications.

Acknowledgement

The authors gratefully acknowledge the National Science Council of the Republic of China for financial support under Contract NSC102-2221-E-007-049-MY3.

Appendix A. Supplementary data

Supplementary data associated with this article can be found, in the online version, at <http://dx.doi.org/10.1016/j.apcatb.2015.08.014>.

References

- [1] P. Wang, B. Huang, X. Qin, X. Zhang, Y. Dai, J. Wei, M.H. Whangbo, Ag@AgCl: a highly efficient and stable photocatalyst active under visible light, *Angew. Chem. Int. Ed.* 47 (2008) 7931–7933.
- [2] H.A. Atwater, A. Polman, Plasmonics for improved photovoltaic devices, *Nat. Mater.* 9 (2011) 205–213.
- [3] P. Christopher, H. Xin, S. Linic, Visible-light-enhanced catalytic oxidation reactions on plasmonic silver nanostructures, *Nat. Chem.* 3 (2011) 467–472.
- [4] X. Li, W.C.H. Choy, L. Huo, F. Xie, W.E.I. Sha, B. Ding, X. Guo, Y. Li, J. Hou, J. You, Y. Yang, Dual plasmonic nanostructures for high performance inverted organic solar cells, *Adv. Mater.* 24 (2012) 3046–3052.
- [5] W. Zhao, Y. Guo, S. Wang, H. He, C. Sun, S. Yang, A novel ternary plasmonic photocatalyst: ultrathin g-C₃N₄ nanosheet hybridized by Ag/AgVO₃ nanoribbons with enhanced visible-light photocatalytic performance, *Appl. Catal. B: Environ.* 165 (2015) 335–343.
- [6] W. Li, C. Feng, S. Dai, J. Yue, F. Hua, H. Hou, Fabrication of sulfur-doped g-C₃N₄ /Au/CdS Z-scheme photocatalyst to improve the photocatalytic performance under visible light, *Appl. Catal. B: Environ.* 168–169 (2015) 465–471.
- [7] H. Li, Y. Sun, B. Cai, S. Gan, D. Han, L. Niu, T. Wu, Hierarchically Z-scheme photocatalyst of Ag@AgCl decorated on BiVO₄ (040) with enhancing photoelectrochemical and photocatalytic performance, *Appl. Catal. B: Environ.* 170–171 (2015) 206–214.
- [8] S. Bouhadoun, C. Guillard, F. Dapozze, S. Singh, D. Amans, J. Bouclé, N. Herlin-Boime, One step synthesis of N-doped and Au-loaded TiO₂ nanoparticles by laser pyrolysis: application in photocatalysis, *Appl. Catal. B: Environ.* 174–175 (2015) 367–375.
- [9] S.C. Warren, E. Thimsen, Plasmonic solar water splitting, *Energy Environ. Sci.* 5 (2012) 5133–5146.

[10] W. Hou, S.B. Cronin, A review of surface plasmon resonance-enhanced photocatalysis, *Adv. Funct. Mater.* 23 (2013) 1612–1619.

[11] K. Awazu, M. Fujimaki, C. Rockstuhl, J. Tominaga, H. Murakami, Y. Ohki, N. Yoshida, T. Watanabe, A plasmonic photocatalyst consisting of silver nanoparticles embedded in titanium dioxide, *J. Am. Chem. Soc.* 130 (2008) 1676–1680.

[12] S.K. Cushing, J. Li, F. Meng, T.R. Senty, S. Suri, M. Zhi, M. Li, A.D. Bristow, N. Wu, Photocatalytic activity enhanced by plasmonic resonant energy transfer from metal to semiconductor, *J. Am. Chem. Soc.* 134 (2012) 15033–15041.

[13] K. Jung, H.J. Song, G. Lee, Y. Ko, K. Ahn, H. Choi, J.Y. Kim, K. Ha, J. Song, J.K. Lee, C. Lee, M. Choi, Plasmonic organic solar cells employing nanobump assembly via aerosol-derived nanoparticles, *ACS Nano* 8 (2014) 2590–2601.

[14] D.B. Ingram, S. Linic, Water splitting on composite plasmonic-metal/semiconductor photoelectrodes: evidence for selective plasmon-induced formation of charge carriers near the semiconductor surface, *J. Am. Chem. Soc.* 133 (2011) 5202–5205.

[15] J. Li, S.K. Cushing, J. Bright, F. Meng, T.R. Senty, P. Zheng, A.D. Bristow, N. Wu, Ag@Cu₂O core-shell nanoparticles as visible-light plasmonic photocatalysts, *ACS Catal.* 3 (2013) 47–51.

[16] Y. Tang, Z. Jiang, G. Xing, A. Li, P.D. Kanhere, Y. Zhang, T.C. Sum, S. Li, X. Chen, Z. Dong, Z. Chen, Efficient Ag@AgCl cubic cage photocatalysts profit from ultrafast plasmon-induced electron transfer processes, *Adv. Funct. Mater.* 23 (2013) 2932–2940.

[17] H.M. Chen, C.K. Chen, M.L. Tseng, P.C. Wu, C.M. Chang, L.C. Cheng, H.W. Huang, T.S. Chan, D.W. Huang, R.S. Liu, D.P. Tsai, Plasmonic ZnO/Ag embedded structures as collecting layers for photogenerating electrons in solar hydrogen generation photoelectrodes, *Small* 9 (2013) 2926–2936.

[18] Z.W. Seh, S. Liu, M. Low, S.Y. Zhang, Z. Liu, A. Mlayah, M.Y. Han, Janus Au-TiO₂ photocatalysts with strong localization of plasmonic near-fields for efficient visible-light hydrogen generation, *Adv. Mater.* 24 (2012) 2310–2314.

[19] Y.C. Pu, G. Wang, K.D. Chang, Y. Ling, Y.K. Lin, B.C. Fitzmorris, C.M. Liu, X. Lu, Y. Tong, J.Z. Zhang, Y.J. Hsu, Y. Li, Au nanostructure-decorated TiO₂ nanowires exhibiting photoactivity across entire uv-visible region for photoelectrochemical water splitting, *Nano Lett.* 13 (2013) 3817–3823.

[20] S. Mukherjee, F. Libisch, N. Large, O. Neumann, L.V. Brown, J. Cheng, J.B. Lassiter, E.A. Carter, P. Nordlander, N.J. Halas, Hot electrons do the impossible: plasmon-induced dissociation of H₂ on Au, *Nano Lett.* 13 (2013) 240–247.

[21] Z. Liu, W. Hou, P. Pavaskar, M. Aykol, S.B. Cronin, Plasmon resonant enhancement of photocatalytic water splitting under visible illumination, *Nano Lett.* 11 (2011) 1111–1116.

[22] H. Gao, C. Liu, H.E. Jeong, P. Yang, Plasmon-enhanced photocatalytic activity of iron oxide on gold nanopillars, *ACS Nano* 6 (2012) 234–240.

[23] G.A. Sotiriou, F.S.A. Dasargyri, M.C. Wurnig, F. Krumeich, A. Boss, J.C. Leroux, S.E. Pratsinis, Photothermal killing of cancer cells by the controlled plasmonic coupling of silica-coated Au/Fe₂O₃ nanoaggregates, *Adv. Funct. Mater.* 24 (2014) 2818–2827.

[24] X. Wang, K.Q. Peng, Y. Hu, F.Q. Zhang, B. Hu, L. Li, M. Wang, X.M. Meng, S.T. Lee, Silicon/hematite core/shell nanowire array decorated with gold nanoparticles for unbiased solar water oxidation, *Nano Lett.* 14 (2014) 18–23.

[25] J. Li, S.K. Cushing, P. Zheng, F. Meng, D. Chu, N. Wu, Plasmon-induced photonic and energy-transfer enhancement of solar water splitting by a hematite nanorod array, *Nat. Commun.* 4 (2013) 1–8.

[26] Y.K. Lin, H.W. Ting, C.Y. Wang, S. Gwo, L.J. Chou, C.J. Tsai, L.J. Chen, Au nanocrystal array/silicon nanoantennas as wavelength-selective photoswitches, *Nano Lett.* 13 (2013) 2723–2731.

[27] S. Mukherjee, L. Zhou, A.M. Goodman, N. Large, C. Ayala-Orozco, Y. Zhang, P. Nordlander, N.J. Halas, Hot-electron-induced dissociation of H₂ on gold nanoparticles supported on SiO₂, *J. Am. Chem. Soc.* 136 (2014) 64–67.

[28] J. Qui, G. Zeng, P. Pavaskar, Z. Li, S.B. Cronin, Plasmon-enhanced water splitting on TiO₂-passivated GaP photocatalysts, *Phys. Chem. Chem. Phys.* 16 (2014) 3115–3121.

[29] H.M. Chen, C.K. Chen, C.J. Chen, L.C. Cheng, P.C. Wu, B.H. Cheng, Y.Z. Ho, M.L. Tseng, Y.Y. Hsu, T.S. Chan, J.F. Lee, R.S. Liu, D.P. Tsai, Plasmon inducing effects for enhanced photoelectrochemical water splitting: X-ray absorption approach to electronic structures, *ACS Nano* 6 (2012) 7362–7372.

[30] Y. Qu, R. Cheng, Q. Su, X. Duan, Plasmonic enhancements of photocatalytic activity of Pt/n-Si/Ag photodiodes using Au/Ag core/shell nanorods, *J. Am. Chem. Soc.* 133 (2011) 16730–16733.

[31] Y. Xia, Y. Xiong, B. Lim, S.E. Skrabalak, Shape-controlled synthesis of metal nanocrystals: simple chemistry meets complex physics, *Angew. Chem. Int. Ed.* 48 (2009) 60–103.

[32] X. Xia, Y. Wang, A. Ruditskiy, Y. Xia, 25th Anniversary article: galvanic replacement: a simple and versatile route to hollow nanostructures with tunable and well-controlled properties, *Adv. Mater.* 25 (2013) 6313–6333.

[33] K.H. Su, Q.H. Wei, X. Zhang, Interparticle coupling effects on plasmon resonances of nanogold particles, *Nano Lett.* 3 (2003) 1087–1090.

[34] H. Wang, T. You, W. Shi, J. Li, L. Guo, Au/TiO₂/Au as a plasmonic coupling photocatalyst, *J. Phys. Chem. C* 116 (2012) 6490–6494.

[35] H. Tang, G. Meng, Q. Huang, Z. Zhang, Z. Huang, C. Zhu, Arrays of cone-shaped ZnO Nanorods decorated with Ag nanoparticles as 3D surface-enhanced raman scattering substrates for rapid detection of trace polychlorinated biphenyls, *Adv. Funct. Mater.* 22 (2012) 218–224.

[36] T. Kawakaki, Y. Takahashi, T. Tatsuma, Enhancement of dye-sensitized photocurrents by gold nanoparticles: effects of plasmon coupling, *J. Phys. Chem. C* 117 (2013) 5901–5907.

[37] S. Linic, P. Christopher, D.B. Ingram, Plasmonic-metal nanostructures for efficient conversion of solar to chemical energy, *Nat. Mater.* 10 (2011) 911–921.

[38] B.F. Mangelson, M.R. Jones, D.J. Park, C.M. Shade, G.C. Schatz, C.A. Mirkin, Synthesis and characterization of a plasmonic–semiconductor composite containing rationally designed, optically tunable gold nanorod dimers and anatase TiO₂, *Chem. Mater.* 26 (2014) 3818–3824.

[39] J.J. Wu, C.H. Tseng, Photocatalytic properties of nc-Au/ZnO nanorod composites, *Appl. Catal. B: Environ.* 66 (2006) 51–57.

[40] P. Thiagarajan, H.J. Ahn, J.S. Lee, J.C. Yoon, J.H. Jang, Hierarchical metal/semiconductor nanostructure for efficient water splitting, *Small* 9 (2013) 2341–2347.

[41] Q. Lu, Z. Lu, Y. Lu, L. Lv, Y. Ning, H. Yu, Y. Hou, Y. Yin, Photocatalytic Synthesis and photovoltaic application of Ag-TiO₂ nanorod composites, *Nano Lett.* 13 (2013) 5698–5702.

[42] S. Sundararajan, N.K. Grady, N. Mirin, N.J. Halas, Nanoparticle-induced enhancement and suppression of photocurrent in a silicon photodiode, *Nano Lett.* 8 (2008) 624–630.

[43] C.K.N. Peh, L. KE, G.W. Ho, Modification of ZnO nanorods through Au nanoparticles surface coating for dye-sensitized solar cells applications, *Mater. Lett.* 64 (2010) 1372–1375.

[44] S.Y. Lin, Y.T. Tsai, C.C. Chen, C.M. Lin, C.H. Chen, Two-step functionalization of neutral and positively charged thiols onto citrate-stabilized Au nanoparticles, *J. Phys. Chem. B* 108 (2004) 2134–2139.

[45] C.N.R. Rao, G.U. Kulkarni, P.J. Thomas, P.P. Edwards, Size-dependent chemistry: properties of nanocrystals, *Chem. Eur. J.* 8 (2002) 28–35.

[46] K.S. Leschkies, R. Divakar, J. Basu, E. Enache-Pommer, J.E. Boercker, C.B. Carter, U.R. Kortshagen, D.J. Norris, E.S. Aydin, Photosensitization of ZnO nanowires with CdSe quantum dots for photovoltaic devices, *Nano Lett.* 7 (2007) 1793–1798.

[47] A. Tanaka, A. Ogino, M. Iwaki, K. Hashimoto, A. Ohnuma, F. Amano, B. Ohtani, H. Kominami, Gold-Titanium(IV) oxide plasmonic photocatalysts prepared by a colloid-photodeposition method: correlation between physical properties and photocatalytic activities, *Langmuir* 28 (2012) 13105–13111.

[48] A.A. Ismail, D.W. Bahnemann, I. Bannat, M. Wark, Gold nanoparticles on mesoporous interparticle networks of titanium dioxide nanocrystals for enhanced photonic efficiencies, *J. Phys. Chem. C* 113 (2009) 7429–7435.

[49] C.C. Lin, Y.C. Yeh, C.Y. Yang, C.L. Chen, G.F. Chen, C.C. Chen, Y.C. Wu, Selective binding of mannose-encapsulated gold nanoparticles to type I Pili in *Escherichia coli*, *J. Am. Chem. Soc.* 124 (2002) 3508–3509.

[50] R.K. Gupta, D.Y. Kusuma, P.S. Lee, M.P. Srinivasan, Covalent assembly of gold nanoparticles for nonvolatile memory applications, *ACS Appl. Mater. Interfaces* 3 (2011) 4619–4625.

[51] X. Yan, C. Zou, X. Gao, W. Gao, ZnO/TiO₂ core–brush nanostructure: processing, microstructure and enhanced photocatalytic activity, *J. Mater. Chem.* 22 (2012) 5629–5640.

[52] C.Y. Kao, C.L. Hsin, C.W. Huang, S.Y. Yu, C.W. Wang, P.H. Yeh, W.W. Wu, High-yield synthesis of ZnO nanowire arrays and their opto-electrical properties, *Nanoscale* 4 (2012) 1476–1480.

[53] C. Zhang, M. Shao, F. Ning, S. Xu, Z. Li, M. Wei, D.G. Evans, X. Duan, Au nanoparticles sensitized ZnO nanorod/nanoplatelet core–shell arrays for enhanced photoelectrochemical water splitting, *Nano Energy* 12 (2015) 231–239.

[54] E. Ha, L.Y.S. Lee, J. Wang, F. Li, K.Y. Wong, S.C.E. Tsang, Significant enhancement in photocatalytic reduction of water to hydrogen by Au/Cu₂ZnSnS₄ nanostructure, *Adv. Mater.* 26 (2014) 3496–3500.

[55] L. Sun, D. Zhao, Z. Song, C. Shan, Z. Zhang, B. Li, D. Shen, Gold nanoparticles modified ZnO nanorods with improved photocatalytic activity, *Colloid Interface Sci.* 363 (2011) 175–181.

[56] M. Murdoch, G.I.N. Waterhouse, M.A. Nadeem, J.B. Metson, M.A. Keane, R.F. Howe, J. Llorca, H. Idriss, The effect of gold loading and particle size on photocatalytic hydrogen production from ethanol over Au/TiO₂ nanoparticles, *Nat. Chem.* 3 (2011) 489–490.

[57] J.W. Chiu, S.C. Ray, H.M. Tsai, C.W. Pao, F.Z. Chien, W.F. Pong, H. Tseng, J.J. Wu, M.H. Tsai, H. Chen, H.J. Lin, J.F. Lee, J.H. Guo, Correlation between electronic structures and photocatalytic activities of nanocrystalline-(Au, Ag, and Pt) particles on the surface of ZnO nanorods, *J. Phys. Chem. C* 115 (2011) 2650–2655.

[58] J.R. Adleman, D.A. Boyd, D.G. Goodwin, D. Psaltis, Heterogenous catalysis mediated by plasmon heating, *Nano Lett.* 9 (2009) 4417–4423.

[59] D.G. Moon, J.H. Yun, J. Gwak, S.K. Ahn, A. Cho, K. Shin, K. Yoon, S. Ahn, Cu_{(In,Ga)Se₂} thin films without Ga segregation prepared by the single-step selenization of sputter deposited Cu-In-Ga-Se precursor layers, *Energy Environ. Sci.* 5 (2012) 9914–9921.

[60] R. Huang, H.C. Ding, W.L. Liang, Y.C. Gao, X.D. Tang, Q. He, C.G. Duan, Z. Zhu, J. Chu, C.A.J. Fisher, T. Hirayama, Y. Ikuhara, Y.H. Chu, Atomic-scale visualization of polarization pinning and relaxation at coherent BiFeO₃/LaAlO₃ interfaces, *Adv. Funct. Mater.* 24 (2014) 793–799.

[61] I.J. Plante, A. Teitelboim, I. Pinkas, D. Oron, T. Mokari, Exciton quenching due to copper diffusion limits the photocatalytic activity of CdS/Cu₂S nanorod heterostructures, *J. Phys. Chem. Lett.* 5 (2014) 590–596.

[62] X. An, X. Yu, J.C.G. Yu, Zhang, Cds nanorods/reduced graphene oxide nanocomposites for photocatalysis and electrochemical sensing, *J. Mater. Chem. A* 1 (2013) 5158–5164.